Chemistry–A European Journal
Research Article
doi.org/10.1002/chem.202203220
Chemistry Europe
European Chemical Societies Publishing
www.chemeurj.org

POM@ZIF Derived Mixed Metal Oxide Catalysts for Sustained Electrocatalytic Oxygen Evolution

Yupeng Zhao,[a, b] Dandan Gao,[a, b] Si Liu,[b] Johannes Biskupek,[c] Ute Kaiser,[c] Rongji Liu,*[a, b, d] and Carsten Streb*[a, b, d]

Abstract: The design of efficient and stable oxygen evolution reaction (OER) catalysts based on noble-metal-free materials is crucial for energy conversion and storage. In this work, it was demonstrated how polyoxometalate (POM)-doped ZIF-67 can be converted into a stable oxygen evolution electrocatalyst by chemical etching, cation exchange, and thermal annealing steps. Characterization by X-ray photoelectron spectroscopy, transmission electron microscopy, energy-dispersive X-ray spectroscopy and Raman spectroscopy indicate that POM-doped ZIF-67 derived carbon-supported metal oxides were synthesized. The resulting composite shows structural and compositional advantages which lead to low overpotential (306 mV at $j = 10\ mA \cdot cm^{-2}$) and long-term stability under harsh OER conditions (1.0 M aqueous KOH).

Introduction

Electrochemical splitting of water into oxygen and hydrogen is one of the most promising large-scale solutions for converting and storing electrical energy.[1–4] Technological implementation and scale-up of this process is hindered, particularly as the oxygen evolution reaction (OER) is demanding, as it involves the proton-coupled transfer of four electrons, operates under harsh oxidative conditions, and often shows slow reaction kinetics.[5–7] Developing effective oxygen evolution catalysts (OECs) is therefore crucial to improve conversion efficiency from intermittent electrical to storable chemical energy. While early studies have focused on understanding the performance of RuO_2 and IrO_2 electrocatalysts,[8,9] recent research has centered on developing robust catalysts based on earth-abundant metals.[5,7,10–13] Recently, composites based on zeolitic imidazolate frameworks (ZIFs) and polyoxometalates (POMs) have gained widespread attention as promising OER catalysts.[4,14–16] Specifically, ZIF-67 shows ordered porosity and high specific surface area,[17] making it ideal for the doping with POMs which can introduce reversible multi-electron redox behaviors.[4] In addition, ZIF-67 is constructed around OER-active Co^{2+} metal nodes. Based on these concepts, a large number of studies have explored the depositing of POMs into ZIFs pores to access OER-active materials. For example, $[H_6CoW_{12}O_{40}]$@ZIF-8 shows stable OER properties at neutral pH;[10] also, TBA-$SiW_{11}CoO_{39}$@ZIF-67 exhibits enhanced OER activities compared with pristine ZIF-67,[17] and similarly, OER activity of TBA-SiW_9Co_3@ZIF-67 is increased when compared with that of the non-modified ZIF-67.[18] Despite this progress, there are still major challenges in the field of POM@ZIFderived OER catalysts. One challenge is that in native ZIFs, most active sites (i.e. metal nodes and embedded POMs) are confined in the inside of the framework,[19] making access by the water substrate and release of the gaseous O_2 product difficult, resulting in often limited performance.[20] Also, both POMs and ZIFs are poor electrical conductors, so that electrocatalytic performance is limited due to high internal resistance.[1] Finally, POMs are unstable in alkaline solutions and most POMs spontaneously degrade at $pH > 8$. Similarly, ZIFs are prone to degradation under electrochemical conditions in alkaline media. This can result in the conversion of Co^{2+} from ZIF-67 to α-$Co(OH)_2$ and β-$Co(OH)_2$, followed by the formation of their corresponding oxidized forms (CoOOH),[21,22] while the original frameworks collapse and lose their porosity.[23,24] As these chemical and structural changes generally lead to low catalytic activity, various conversion routes have been developed to access more robust, more active POM@ZIF derived composites, leading to metal oxides,[25] metal sulfides,[26] metal carbides,[27] and metal phosphides.[28,29] Often, these composites combine increased

[a] Y. Zhao, Dr. D. Gao, Dr. R. Liu, Prof. Dr. C. Streb
Department of Chemistry
Johannes Gutenberg University Mainz
Duesbergweg 10–14, 55131 Mainz (Germany)
E-mail: rongji.liu@uni-mainz.de
carsten.streb@uni-mainz.de
Homepage: https://www.strebgroup.net/
[b] Y. Zhao, Dr. D. Gao, Dr. S. Liu, Dr. R. Liu, Prof. Dr. C. Streb
Institute of Inorganic Chemistry I
Ulm University
Albert-Einstein-Allee 11, 89081 Ulm (Germany)
[c] Dr. J. Biskupek, Prof. Dr. U. Kaiser
Central Facility of Electron Microscopy for Materials Science
Ulm University
Albert-Einstein-Allee 11, 89081 Ulm (Germany)
[d] Dr. R. Liu, Prof. Dr. C. Streb
Helmholtz-Institute Ulm
Electrochemical Energy Conversion
Helmholtzstrasse 11, 89081 Ulm (Germany)

Supporting information for this article is available on the WWW under https://doi.org/10.1002/chem.202203220

electrical conductivity with chemical and mechanical stability, making them interesting new OER catalysts.

Here, we report a facile chemical route to convert POM-doped ZIF-67, giving access to a noble metal-free OER catalyst using a combination of acid etching followed by cation-exchange and thermal annealing. The route enables conversion of the original $[H_3PW_{12}O_{40}]$-doped amorphous ZIF-67 (PW_{12}@amZIFs) into carbon-supported metal oxide composites. The catalyst shows excellent OER performance in 1 M aqueous KOH electrolyte with sustained electrochemical activity. This work presents a facile approach to produce high performance electrocatalyst composite for OER in alkaline media.

Results and Discussion

The synthesis process, using a weak acid-assisted etching and subsequent ion exchange and thermal annealing is presented in Figure 1. Briefly, amorphous POM doped ZIF-67 (PW_{12}@amZIF) was prepared via a facile in situ method (details in the Supporting Information). To improve porosity and pore accessibility, the native PW_{12}@amZIF was etched with tannic acid.[20] Next, Ni^{2+} and Fe^{3+} were introduced into the system by a cation exchange process. The final product was obtained after annealing at 300 °C in air for 3 h, and labelled **Catalyst 1**. For synthetic details, see the Supporting Information. To understand the synergistic effect of the presence of multiple metal reaction sites, catalysts without W, Fe, and Ni were also prepared for as reference materials, and labelled **Catalyst 2** (without W), **Catalyst 3** (without Fe), and **Catalyst 4** (without Ni), respectively.

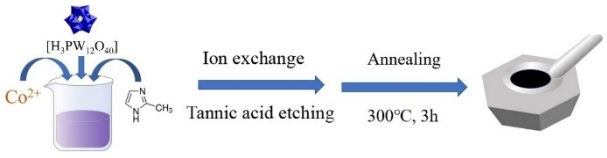

Figure 1. schematic materials design and fabrication approach.

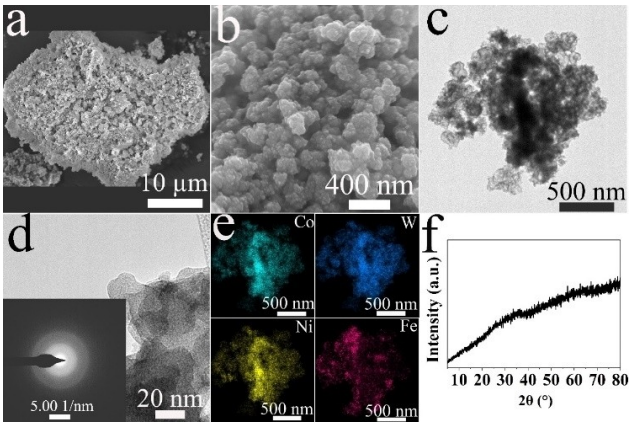

Figure 2. Structural and compositional analysis of **Catalyst 1**: (a and b) SEM images at low and high magnification. (c and d) TEM and HRTEM images with insert of SAED pattern. (e) STEM-EDX elemental mappings (f) pXRD pattern.

Scanning electron microscopy (SEM), aberration-corrected high-resolution transmission electron microscopy (HRTEM), and scanning transmission electron microscopy (STEM) were employed to examine the morphology of **Catalyst 1** and its precursor PW_{12}@amZIF. The resulting HRTEM image (Figure 2c) reveals that **Catalyst 1** possesses a hollow structure that does not exist in the pristine PW_{12}@amZIF. We assign the formation of these hollow structures to the tannic acid etching, as similar properties have been reported previously in tannic acid-etched materials.[20] Also, the particle size of **Catalyst 1** (Figure 2a, b) is larger than PW_{12}@amZIF (Figure S1a, b), suggesting that aggregation occurred during the cation-exchange and thermal annealing, resulting in low specific surface area. For **Catalyst 1**, no obvious lattice fringes are observed in HRTEM (Figure 2d) and the corresponding selected area electron diffraction (SAED) pattern (Figure 2d insert) only shows an obvious halo, which indicates their amorphous structure[30] and is in agreement with the powder X-ray diffraction (pXRD) data (Figure 2f). Energy-dispersive X-ray spectroscopy (EDX)-STEM elemental mappings (Figure 2e) verify the presence of homogeneously dispersed W, Co, Ni, and Fe within the catalyst. This indicates that the Ni and Fe ion exchange into the material was successful and led to a homogeneous distribution of these metal ions. To gain more composition information of **Catalyst 1**, inductively coupled plasma optical emission spectroscopy (ICP-OES, Table S1) was employed as well and gave an approximate atomic ratio of 1 : 1.1 : 2 : 0.2 (Ni/W/Co/Fe).

The elemental oxidation states of **Catalyst 1** were studied by X-ray photoelectron spectroscopy (XPS). The survey XPS spectrum (Figure 3a) indicates the presence of O, C, W, Co, Ni, and Fe. The deconvoluted high-resolution W 4f XPS spectrum (Figure 3b) suggests the presence of W^{6+} in **Catalyst 1** (35.34 eV for W $4f_{7/2}$ and 37.51 eV for W $4f_{5/2}$).[31] XPS analysis also suggests that both, Ni (Figure 3c) and Fe (Figure 3d) are present in oxidation state +3 (856.07 eV for Ni $2p_{3/2}$ and 873.37 eV for Ni $2p_{1/2}$; 711 eV for Fe $2p_{3/2}$ and 724 eV for Fe $2p_{1/2}$). In contrast, XPS analysis for cobalt (Figure 3e), suggest mixed

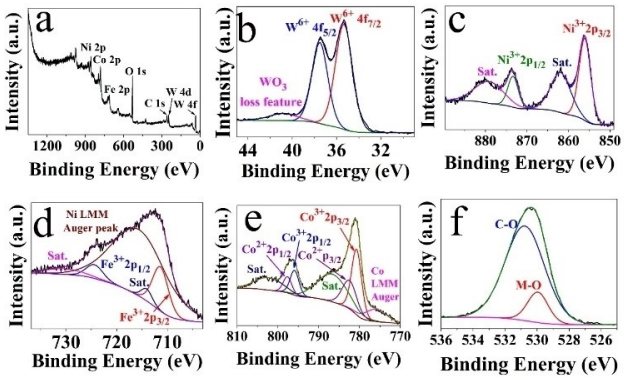

Figure 3. XPS spectra of **Catalyst 1**: (a) overview spectrum, (b-f) deconvoluted high-resolution spectra of W 4f (b), Ni 2p (c), Fe 2p (d), Co 2p (e), and (f) O 1s.

$Co^{2+/3+}$ oxidation states as indicated by the characteristic signals at 780.7 eV ($2p_{3/2}$ for Co^{3+}) and 782.4 eV ($2p_{3/2}$ for Co^{2+}).[32] The molar ratio of Co^{3+}: Co^{2+} is approx. 1.6: 1. The deconvoluted XPS spectrum for O 1s (Figure 3f) indicates two distinct signals assigned to metal oxide and carbon oxygen species. The presence of metal oxide species is further indicated by characteristic signals in the Raman spectrum of **Catalyst 1** (Figure S2). Further, Raman spectroscopy also showed two intense signals at 1313 cm^{-1} and 1586 cm^{-1}, corresponding to the D and G bands of the carbon matrix.[33,34] The obtained results indicate that the organic imidazole ligands of the ZIF have been converted into carbonaceous compounds after thermal annealing, which act as heterogeneous support for the metal oxides formed.

Next, we investigated the electrochemical activity of **Catalyst 1** in alkaline aqueous solution (1 M aqueous KOH, pH = 13.7) with a standard three-electrode electrochemical setup, in which Hg/HgO was used as reference electrode and platinum foil as the counter electrode. The catalysts were drop-cast on a glassy carbon rotating disk electrode (RDE) which was used as working electrode. All potentials were converted to reversible hydrogen electrode potentials (RHE, see details in Supporting Information). The OER electrocatalytic performance was assessed by linear sweep voltammetry (LSV) at a scan rate of 5 $mV \cdot s^{-1}$. **Catalyst 1** shows the best performance for OER with an overpotential of $\eta = 306$ mV at the current density of $j = 10\ mA \cdot cm^{-2}$ (Figure 4a, b). In contrast, **Catalyst 2**, **Catalyst 3**, and **Catalyst 4** show significantly higher overpotentials at the current density of $j = 10\ mA \cdot cm^{-2}$. Tafel plot analysis (η versus log(j)) was used to assess the OER kinetics (Figure 4c). Amongst the materials compared, **Catalyst 1** shows the lowest Tafel slope (54 $mV \cdot dec^{-1}$), while the reference samples show slightly higher Tafel slopes, suggesting that OER is kinetically favored in **Catalyst 1** compared with the reference samples.

To gain deeper insights into the reaction mechanism of **Catalyst 1**, rotating ring-disk electrode (RRDE) voltammetry was used. While the OER reaction was performed at the disk electrode, the Pt ring electrode (at $E = 1.5$ V) was used to oxidize and detect any partially oxidized intermediates formed, such as H_2O_2 (see details in Supporting Information). Under the given conditions, only a very low ring current (μA scale) was detected, which indicates that peroxide intermediate formation is negligible, so that **Catalyst 1** favors the preferred 4-electron OER pathway (Figure S3). The faradaic efficiency of **Catalyst 1** was also assessed using RRDE voltammetry. Here, the ring potential was set to $E = 0.40$ V, so that any oxygen formed by OER on the disk electrode is reductively detected at the ring electrode (Figure 4d). Based on the observed ring current (~21 μA, current collection efficiency: 0.15) and disk current (~147 μA), we were able to calculate an OER faradaic efficiency of 94.3% for **Catalyst 1** (detailed calculation in the Supporting Information).

The double-layer capacitance (C_{dl}), which is proportional to the electrochemically active surface area (ECSA), and electrochemical impedance spectroscopy (EIS) were used to gain a deeper understanding of the electrocatalytic performance. The resulting C_{dl} indicates **Catalyst 1** exhibited comparable ECSAs with other reference catalysts **2**, **3** and **4** (Figure S4 and Figure 4e). In contrast, EIS analysis indicates that **Catalyst 1** features the lowest charge transfer resistance (R_{ct}) among the catalysts studied, which leads to efficient interfacial electron transfer (Figure S5). Thus, the high OER performance of **Catalyst 1** is due to low internal charge transfer resistance as well as high intrinsic reactivity of the catalyst.

Next, we examined the long-term stability of **Catalyst 1** under a given operating condition (1 M KOH, $\eta = 340$ mV) using chronoamperometry. In this case, the catalyst was dropped on carbon paper which is chemically stable under OER conditions. As shown in Figure 4f, the value of j increases by 29.3% during the initial first hour. Then it reaches a maximum and drops slightly (ca. 3%) over the following 14 h. We suggest that the initial increase of j is due to chemical and morphological changes of the catalyst, which was studied by post-catalytic STEM-EDX analyses (Figure S6). The elemental mapping reveals that Co, Ni, and O are still distributed homogeneously and that there are no crystalline Co and Ni-based composites present. However, for W and Fe, aggregation is observed and some sheet-like crystalline structures are formed. These are identified as Fe_2O_3 by SAED (lattice spacing) and EDX (elemental ratio between Fe and O). Based on earlier reports, this formation could contribute to the catalytic activity of the catalyst.[35] Also, post-catalytic XPS analysis of **Catalyst 1** indicates that the Co^{2+} ions are oxidized to more OER-active Co^{3+} species during the catalytic process (Figure S7).[22] These factors contribute to the observed behavior during the chronoamperometric analysis.

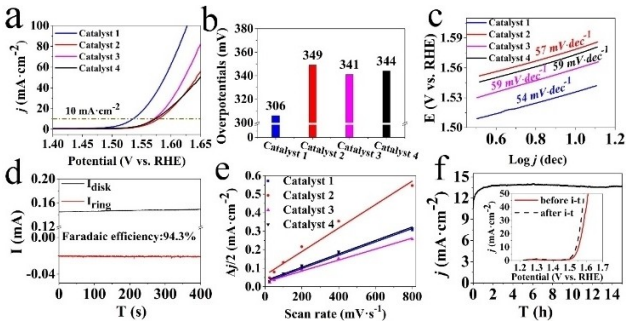

Figure 4. Electrocatalytic OER performance of **Catalyst 1** and reference catalysts in 1 M aqueous KOH: a) iR-corrected OER polarization curves, b) Overpotentials at $j = 10\ mA \cdot cm^{-2}$, c) Tafel plot, d) RRDE analysis to determine faradaic efficiency for **Catalyst 1**, e) Half of the capacitive current density ($\Delta j/2$) at 0.87 V vs. RHE as a function of the scan rates and f) Chronoamperometry curves at $\eta = 340$ mV (insert: LSV polarization curves comparison before and after 15 h stability test).

Conclusion

A facile design route for the synthesis of noble-metal-free OER catalysts was reported. Structural and compositional synergisms lead to enhanced electrocatalytic OER performance with low overpotential (306 mV at $j = 10\ mA \cdot cm^{-2}$), high faradaic efficiency (94.3%), and a Tafel slope of 54 $mV \cdot dec^{-1}$. The catalyst shows long-term robustness and offers a new path for the

scalable design of OER electrocatalysts based on earth-abundant components.

Experimental Section

Synthesis PW_{12}@amZIF: In a typical synthesis, aqueous $[H_3PW_{12}O_{40}]\cdot xH_2O$ solution (0.07 mmol in 10 mL) was added to $Co(NO_3)_2\cdot 6H_2O$ (0.546 g, 1.8 mmol) methanol solution (25 mL) and kept under magnetic stirring for 0.5 h. Afterward, 2-methylimidazole (0.616 g, 7.5 mmol) methanol solution (25 mL) was added. This reaction was stirred for another 2.5 h. The final, solid product was collected by centrifugation, washed with methanol, and dried at 70 °C overnight.

Acid etching: PW_{12}@amZIF: 150 mg of PW_{12}@amZIF was dispersed in 5 ml of ethanol by sonication for 20 min. The dispersion was added into ethanol/ DI water (10 mL: 15 mL) solution containing 75 mg of tannic acid. The solution was stirred for 10 minutes. Finally, the material was collected via centrifugation, washing with ethanol, and drying at 70 °C overnight.

Metal ions exchange: 50 mg of acid etched material was dispersed in 10 ml of ethanol. Then 24 ml of DI water containing 2.5 mM $NiCl_2$ and 0.25 mM $FeCl_3$ were added dropwise. Finally, the solution was stirred at room temperature for 3 h and the material was collected via centrifugation, washing with ethanol, and drying at 70 °C overnight.

Annealing process: The as-prepared material was annealed in air at 300 °C for 3 h with a heating rate of 5 °C·min^{-1} and natural cool-down to room temperature

Acknowledgements

The authors gratefully acknowledge financial support by the Deutsche Forschungsgemeinschaft DFG (Cluster of Excellence EXC2154, POLiS, project number: 390874152 and TRR 234 CataLight, project number: 364549901 and project no 389183496). R.L. gratefully acknowledges financial support by the Alexander von Humboldt Foundation. R.L., D.G. and C.S. gratefully acknowledge financial support by Johannes Gutenberg University Mainz, the Rheinland-Pfalz Research Initiative SusInnoScience and the Gutenberg Research College. Open Access funding enabled and organized by Projekt DEAL.

Conflict of Interest

The authors declare no conflict of interest.

Data Availability Statement

The data that support the findings of this study are available from the corresponding author upon reasonable request.

Keywords: composites · electrocatalysis · metal oxides · oxygen evolution reactions · polyoxometalates

[1] H. Wen, S. Zhang, T. Yu, Z. Yi, R. Guo, *Nanoscale* **2021**, *13*, 12058–12087.
[2] T. Reier, M. Oezaslan, P. Strasser, *ACS Catal.* **2012**, *2*, 1765–1772.
[3] S. Yang, J. Y. Zhu, X. N. Chen, M. J. Huang, S. H. Cai, J. Y. Han, J. sen Li, *Appl. Catal. B* **2022**, *304*, 120914.
[4] W. Luo, J. Hu, H. Diao, B. Schwarz, C. Streb, Y. F. Song, *Angew. Chem. Int. Ed.* **2017**, *56*, 4941–4944; *Angew. Chem.* **2017**, *129*, 5023–5026.
[5] W. Li, S. Watzele, H. A. El-Sayed, Y. Liang, G. Kieslich, A. S. Bandarenka, K. Rodewald, B. Rieger, R. A. Fischer, *J. Am. Chem. Soc.* **2019**, *141*, 5926–5933.
[6] H. Lv, Y. v. Geletii, C. Zhao, J. W. Vickers, G. Zhu, Z. Luo, J. Song, T. Lian, D. G. Musaev, C. L. Hill, *Chem. Soc. Rev.* **2012**, *41*, 7572–7589.
[7] B. Rausch, M. D. Symes, G. Chisholm, L. Cronin, *Science* **2014**, *345*, 1326–1330.
[8] R. Samanta, P. Panda, R. Mishra, S. Barman, *Energy Fuels* **2022**, *36*, 1015–1026.
[9] Y. Lee, J. Suntivich, K. J. May, E. E. Perry, Y. Shao-Horn, *J. Phys. Chem. Lett.* **2012**, *3*, 399–404.
[10] S. Mukhopadhyay, J. Debgupta, C. Singh, A. Kar, S. K. Das, *Angew. Chem. Int. Ed.* **2018**, *57*, 1918–1923; *Angew. Chem.* **2018**, *130*, 1936–1941.
[11] B. Y. Xia, Y. Yan, N. Li, H. bin Wu, X. W. D. Lou, X. Wang, *Nat. Energy* **2016**, *1*, 1–8.
[12] X. F. Lu, Y. Fang, D. Luan, X. W. D. Lou, *Nano Lett.* **2021**, *21*, 1555–1565.
[13] Y. Liu, D. Zhou, T. Deng, G. He, A. Chen, X. Sun, Y. Yang, P. Miao, *ChemSusChem* **2021**, *14*, 5359–5383.
[14] M. Blasco-Ahicart, J. Soriano-Lopez, J. J. Carbo, J. M. Poblet, J. R. Galan-Mascaros, *Nat. Chem.* **2018**, *10*, 24–30.
[15] J. Li, S. Gadipelli, *Chem. Eur. J.* **2020**, *26*, 14167–14172.
[16] S. L. Zhang, B. Y. Guan, X. F. Lu, S. Xi, Y. Du, X. W. Lou, *Adv. Mater.* **2020**, *32*, 2002235.
[17] V. K. Abdelkader-Fernández, D. M. Fernandes, S. S. Balula, L. Cunha-Silva, C. Freire, *J. Mater. Chem. A* **2020**, *8*, 13509–13521.
[18] G. Paille, M. Gomez-Mingot, C. Roch-Marchal, M. Haouas, Y. Benseghir, T. Pino, M. H. Ha-Thi, G. Landrot, P. Mialane, M. Fontecave, A. Dolbecq, C. Mellot-Draznieks, *ACS Appl. Mater. Interfaces* **2019**, *11*, 47837–47845.
[19] J. Li, W. Huang, M. Wang, S. Xi, J. Meng, K. Zhao, J. Jin, W. Xu, Z. Wang, X. Liu, Q. Chen, L. Xu, X. Liao, Y. Jiang, K. A. Owusu, B. Jiang, C. Chen, D. Fan, L. Zhou, L. Mai, *ACS Energy Lett.* **2019**, *4*, 285–292.
[20] C. Wang, J. Zhang, Z. Zhang, G. Ren, D. Cai, *RSC Adv.* **2020**, *10*, 38906–38911.
[21] X. Cai, F. Peng, X. Luo, X. Ye, J. Zhou, X. Lang, M. Shi, *ChemSusChem* **2021**, *14*, 3163–3173.
[22] W. Zheng, M. Liu, L. Y. S. Lee, *ACS Catal.* **2020**, *10*, 81–92.
[23] X. Cai, F. Peng, X. Luo, X. Ye, J. Zhou, X. Lang, M. Shi, *ChemSusChem* **2021**, *14*, 3163–3173.
[24] W. Zheng, M. Liu, L. Y. S. Lee, *ACS Catal.* **2020**, *10*, 81–92.
[25] Z. Kou, W. Zang, Y. Ma, Z. Pan, S. Mu, X. Gao, B. Tang, M. Xiong, X. Zhao, A. K. Cheetham, L. Zheng, J. Wang, *Nano Energy* **2020**, *67*, 104288.
[26] Y. J. Tang, Y. Wang, X. L. Wang, S. L. Li, W. Huang, L. Z. Dong, C. H. Liu, Y. F. Li, Y. Q. Lan, *Adv. Energy Mater.* **2016**, *6*, 1–7.
[27] J. Q. Chi, X. Shang, S. S. Lu, B. Dong, Z. Z. Liu, K. L. Yan, W. K. Gao, Y. M. Chai, C. G. Liu, *Carbon NY* **2017**, *124*, 555–564.
[28] J. sen Li, S. Zhang, J. Q. Sha, H. Wang, M. Z. Liu, L. X. Kong, G. D. Liu, *ACS Appl. Mater. Interfaces* **2018**, *10*, 17140–17146.
[29] J. sen Li, S. Zhang, J. Q. Sha, H. Wang, M. Z. Liu, L. X. Kong, G. D. Liu, *ACS Appl. Mater. Interfaces* **2018**, *10*, 17140–17146.
[30] X. Zhou, L. Yu, X.-Y. Yu, X. Wen, D. Lou, X. Zhou, L. Yu, X. W. Lou, X. Y. Yu, *Adv. Energy Mater.* **2016**, *6*, 1601177.
[31] D. Gao, R. Liu, J. Biskupek, U. Kaiser, Y.-F. Song, C. Streb, *Angew. Chem. Int. Ed.* **2019**, *58*, 4644–4648; *Angew. Chem.* **2019**, *131*, 4692–4696.
[32] L. F. Gu, J. J. Chen, T. Zhou, X. F. Lu, G. R. Li, *Nanoscale* **2020**, *12*, 11201–11208.
[33] S. Wang, Y. Wang, S. Lin Zhang, S.-Q. Zang, X. Wen Lou, S. Wang, Y. Wang, S. L. Zhang, X. W. Lou, S. Zang, *Adv. Mater.* **2019**, *31*, 1903404.
[34] H. Zhang, W. Zhou, F. Lu, T. Chen, X. Wen, D. Lou, H. Zhang, X. F. Lu, D. X. W. Lou, W. Zhou, T. Chen, *Adv. Energy Mater.* **2020**, *10*, 2000882.
[35] D. R. Kauffman, X. Deng, D. C. Sorescu, T. D. Nguyen-Phan, C. Wang, C. M. Marin, E. Stavitski, I. Waluyo, A. Hunt, *ACS Catal.* **2019**, 5375–5382.

Manuscript received: October 14, 2022
Accepted manuscript online: December 2, 2022
Version of record online: February 1, 2023